Clay Minerals (2024), **59**, 179–191
doi:10.1180/clm.2024.18

CAMBRIDGE UNIVERSITY PRESS

Article

Stability performance of an Algerian Ni/purified diatomite catalyst in the dry reforming methane reaction: characterization and properties

Massinissa Adjissa[1], Nedjima Bouzidi[1], Kahina Ikkour[2], Salim Ouhenia[2], Ouarda Benlounes[3] and Nouara Lamrani[3]

[1]Université de Béjaïa, Faculté de Technologie, Laboratoire de Technologie des Matériaux et du Génie des Procédés (LTMGP), Béjaïa, Algeria; [2]Université de Béjaïa, Faculté des Sciences Exactes, Laboratoire de Physico-chimie des Matériaux et Catalyse (LPCMC), Béjaïa, Algeria and [3]Applied Chemistry and Chemical Engineering Laboratory, University of Tizi Ouzou, Tizi Ouzou, Algeria

Abstract

This work aims to characterize and study the properties of an Algerian diatomaceous earth (Sig-Mascara) as a catalyst carrier. A commercial product of diatomite was characterized by granulometric analysis, X-ray fluorescence, X-ray diffraction, Fourier-transform infrared spectroscopy, thermogravimetric analysis/differential scanning calorimetry and scanning electron microscopy/energy-dispersive X-ray spectroscopy methods. To purify the diatomite and remove the impurities (iron oxides, clay minerals, quartz and organic matters), the <63 μm fraction of the diatomite was separated out. The 15Ni/Ds-700 catalyst has lower SiO_2, Al_2O_3 and CaO contents compared with the original diatomite. The NiO content of the catalyst is 15 wt.%, indicating successful impregnation. According to the nitrogen sorption–desorption results, the specific surface area of the purified diatomite particles (<63 μm) increased from 26.47 to 46.33 $m^2\ g^{-1}$ compared to crude diatomite. The 15Ni/Ds-700 catalyst was applied in the dry reforming of methane to obtain synthesis gas (CO and H_2). The results showed that the catalyst was relatively stable during catalytic measurements for 6 h, although the conversion rate value was low (12%).

Keywords: Algerian diatomite, BET characterization, conversion, dry reforming of methane, impregnation method, Ni/diatomite catalyst, nickel, stability

(Received 30 December 2023; revised 27 June 2024; Editor: George Christidis)

Diatomites are naturally abundant materials consisting mainly of SiO_2 (~60–80 wt.%) associated with organic matter (Hao *et al.*, 2021). Thus, they are environmentally friendly biogenic sediments, and they qualify as ecological materials (Fraine *et al.*, 2019; Shen *et al.*, 2021). Diatomite is mainly composed of amorphous silica with an abundant silica hydroxyl group consisting of fossil remains of diatom frustules (Shen *et al.*, 2021). In its pure state, it appears as a fine, white, very porous, lightweight, friable sediment (Taoukil *et al.*, 2021). In the Sig region (Mascara) of north-west Algeria, a diatomite deposit of Miocene age has formed in a lacustrine environment. The diatomite reserves are estimated to be several million tons (Meradi *et al.*, 2015). The Algerian diatomite, also called kieselguhr, has a whitish colour and a high porosity, exceeding 72%.

Diatomite is commonly used in engineering and environmental applications (Xia *et al.*, 2020) as an adsorbent, filter and catalyst support (Yusan *et al.*, 2016; Hao *et al.*, 2021). Previous studies have shown that diatomite is an important support for catalysts that remove heavy metal ions and dyes (Van Viet *et al.*, 2020), in explosives as a stabilizer (Guhr dynamite), as a material for tubular filters, as an insecticide and recently as a building material in the production of bricks (Lauermannová *et al.*, 2021). The periodic pores of diatomite give it advanced characteristics, such as the adsorption capacity and characteristics of photonic crystals at the nanoscale (Shen *et al.*, 2021), and it can be used for thermal insulation due to its low thermal conductivity, as well as for the manufacture of antibiotics and some pharmaceutical syrups (Fraine *et al.*, 2019). Algerian diatomite has many important industrial applications in sustainable and environmentally friendly development (Mansour *et al.*, 2008; Meradi *et al.*, 2015). These applications include the purification of drinking water (Hadjar *et al.*, 2008; Cherrak & Hadjel, 2016), filtration (Hadjar *et al.*, 2011), as abrasive agents and anti-explosive agents (Balaska *et al.*, 2008; Meradi *et al.*, 2016) and as ceramic and insulating materials (Benayache *et al.*, 2018; Aouadja *et al.*, 2022).

In the field of catalysis, diatomite is used as a catalyst support because of its large specific surface area, uniform pore diameter, regular shape and pore sizes ranging from the nanometre to the micrometre scale (Hadjadj-Aoul *et al.*, 2005; Liu *et al.*, 2016; Dekkar *et al.*, 2020; Taoukil *et al.*, 2021). All of these properties of diatoms make this material a very promising candidate for the preparation and synthesis of hierarchical porosity catalyst supports applicable in the field of catalysis and chromatography (Li *et al.*, 2022). The choice of natural resources (aluminosilicates) as support materials is based on their interesting textural properties (specific surface area, pore volume, pore diameter), good

Corresponding author: Nedjima Bouzidi; Email: nedjmabouzidi@yahoo.fr
Cite this article: Adjissa M, Bouzidi N, Ikkour K, Ouhenia S, Benlounes O, Lamrani N (2024). Stability performance of an Algerian Ni/purified diatomite catalyst in the dry reforming methane reaction: characterization and properties. *Clay Minerals* **59**, 179–191. https://doi.org/10.1180/clm.2024.18

catalytic properties, high availability and low cost. The Ni–SiO_2-based catalysts are suitable due to their mechanical resistance, good chemical and thermal stability, low cost and high availability (Dekkar *et al.*, 2020).

The dry reforming of methane (DRM) reaction consumes two main greenhouse gases (methane and carbon dioxide) and produces hydrogen and carbon monoxide in a 1:1 ratio. They can be used directly as raw materials to replace traditional petroleum synthetic chemical products in downstream Fischer–Tropsch synthesis (Raje *et al.*, 1998). Therefore, this appears to be a suitable path for the disposal of both gases, with direct energetic and environmental benefits (Mendoza-Nieto *et al.*, 2018; Abdullah *et al.*, 2021; Sophiana *et al.*, 2022). Although noble metal catalysts, such as Ru, Rh, Pd, Ir and Pt, can achieve better catalytic activity and stability (Pakhare & Spivey, 2014; Qin *et al.*, 2020; Moreno *et al.*, 2021; Niu *et al.*, 2021), their high cost limits their applicability. At present, the active components of methane dry reforming catalysts are mainly transition metals, such as Ni, Co and Fe, and Ni-based catalysts have been the most widely studied in recent decades due to their low cost and high activity.

In this work, a diatomite soil was used as a support for Ni-based catalysts to study its influence on the catalytic reactivity of the generated oxide particles and to test their performance and the possibility of their application in the field of catalysis. The diatomite powder was physically and chemically characterized and the <63 µm fraction was used as a support to remove all impurities that negatively affect the catalyst support. The catalyst was prepared *via* the method of impregnation of Ni on the <63 µm diatomite support, and the whole catalyst system was calcined at 700°C for 2 h. The results of converting methane and CO_2 to synthesis gas (CO and H_2) *via* the gas chromatography method showed that the catalyst was not deactivated after 6 h of catalytic testing, and the conversion rate was estimated at 12%.

Materials and methods

Materials

The Algerian diatomite (commercial product obtained from the Sig mine in Mascara, north-west of Algeria, a diatomite processing factory) was naturally dried for 48 h, crushed with a FRITSCH laboratory-type jaw crusher and then sieved with a series of standardized sieves (2, 1, 0.5, 0.25, 0.125 and 0.063 mm) with a Retsch sieve shaker. The fine fraction of <63 µm was selected as a support to prepare the Ni catalyst. Nickel (II) nitrate hexahydrate ($Ni(NO_3)_2.6H_2O$) was used to prepare a catalyst based on nickel (15% Ni), supported by the diatomite.

To prepare 3 g of 15% Ni catalyst, a suitable mass of $Ni(NO_3)_2.6H_2O$ was dissolved in an appropriate volume of water and then impregnated onto the support. The resulting product was then dried at 100°C for 24 h. At the end of the drying process, a 15% Ni-doped sample was obtained. The resulting material was ground manually in an agate mortar and subsequently calcined at 700°C using a tunnel furnace to produce a catalyst named 15Ni/Ds-700.

Methods

Approximately 50 mg of Ni catalyst supported on diatomite powder was introduced into the middle of a tubular quartz reactor with an internal diameter of 6 mm and intercalated with quartz wool. The catalyst was introduced into the tubular furnace fixed vertically so that the catalyst zone corresponded to the central zone of the furnace under reduced conditions with a pure hydrogen flow (40 mL min^{-1}). The catalytic tests were carried out under a gas stream containing CH_4 and CO_2 (CH_4:CO_2 ratio = 1) with a volume flow rate of 50 mL min^{-1} at 700°C (i.e. 25 mL min^{-1} for each gas). At the end of the reaction, the final quantities of products and reagents were detected using a gas chromatograph (Shimadzu GC-2014).

In the DRM, methane (CH_4) and carbon dioxide (CO_2) react to produce carbon monoxide (CO) and hydrogen (H_2) according to Equation 1:

$$CH_4 + CO_2 \rightleftharpoons 2CO + 2H_2 \quad (1)$$

The conversions of methane and carbon dioxide and H_2:CO ratio were calculated according to Equations 2 & 3:

$$\text{Conversion}\,(X_{CH_4\%}) = \frac{n_{(CH_4)\text{in}} - n_{(CH_4)\text{out}}}{n_{(CH_4)\text{in}}} \times 100 \quad (2)$$

$$\text{Conversion}\,(X_{CO_2\%}) = \frac{n_{(CO_2)\text{in}} - n_{(CO_2)\text{out}}}{n_{(CO_2)\text{in}}} \times 100 \quad (3)$$

This main reaction of Equation 1 is accompanied by intermediate reactions such as methane dissociation, the Boudouard reaction and the water–gas shift reaction. These secondary reactions influence the final CO and H_2 yields according to Equation 4:

$$\text{Yield}\,(Y_{H_2\%}) = \frac{n_{(H_2)\text{out}}}{2n_{(CH_4)\text{in}}} \times 100 \quad (4)$$

where $n_{(H2)\text{out}}$ represents the moles of hydrogen produced and $2n_{(CH4)\text{in}}$ represents the maximum theoretical moles of hydrogen that could be produced from the consumed methane.

As CO is produced from the reaction of methane and carbon dioxide, the CO yield is given according to Equation 5:

$$\text{Yield}\,(Y_{CO\%}) = \frac{n_{(CO)_{\text{out}}}}{n_{(CH_4)\text{in}} + n_{(CO_2)\text{in}}} \times 100 \quad (5)$$

where $n_{(CH4)\text{in}} + n_{(CO2)\text{in}}$ represents the total of the reactants (methane and carbon dioxide) consumed in the reaction.

The H_2:CO molar ratio is calculated according to Equation 6:

$$\text{Molar ratio}\,(H_2{:}CO) = \frac{n_{(H_2)\text{produced}}}{n_{(CO)\text{produced}}} \quad (6)$$

In addition, the carbon balance (X_C) is calculated according to Equation 7:

$$X_C = \frac{n_{(CH_4)\text{out}} + n_{(CO_2)\text{out}}}{n_{(CH_4)\text{in}} + n_{(CO_2)\text{in}}} \times 100 \quad (7)$$

where n expresses the number of moles of CH_4, CO_2, CO and H_2 at the inlet and outlet of the reactor, X_{CH4} and X_{CO2} are the conversion rates of CH_4 and CO_2, respectively, and Y_{H2} and Y_{CO} are the yields of H_2 and CO, respectively.

The H_2:CO^- molar ratio is calculated according to Equation 8:

$$\text{Molar ratio } \frac{H_2}{CO} = \frac{A_{H_2}}{A_{CO}} \quad (8)$$

where

$$A_{H_2} = \frac{F_{CH_{4_{int}}} \times (n_{H_2})_{out}}{m_{cata} \times (n_{CH_4})_{int}}$$

$$A_{CO} = \frac{F_{CH_{4_{int}}} \times (n_{CO})_{out}}{m_{cata} \times (n_{CH_4})_{int}}$$

and A_{H2} is the activity of H_2 (μM/g.s), A_{CO} is the activity of CO (μM/g.s), m_{cata} is the mass of the catalyst (g), $F_{(CH_4)int}$ is the CH_4 flow rate at the reactor inlet (μM s^{-1}), $(n_{CH_4})_{int}$ is the number of moles of CH_4 at the reactor inlet, $(n_{H_2})_{out}$ is the number of moles of H_2 at the outlet of the reactor and $(n_{CO})_{out}$ is the number of moles of CO at the outlet of the reactor.

The following experimental conditions of the DRM reaction were chosen according to the Challiwala *et al.* (2017): reaction temperatures higher than 650°C, atmospheric pressure and CH_4:CO_2 ratio equal to 1. The evolutions of CH_4 and CO_2 conversions over time for the 15Ni/Ds-700 catalysts were recorded under the following conditions: gas hourly space velocity (GHSV) 30 Lh^{-1} g^{-1}, reaction temperature 700°C and reaction time 6 h. The evolutions of CO and H_2 yields and of the H_2:CO ratio over time for the 15 Ni/Ds-700 catalysts were recorded under the following conditions: GHSV 30 Lh^{-1} g^{-1}, reaction temperature 700°C and reaction time 6 h.

Granulometric analysis of crude diatomite

The particle-size distribution of the crude diatomite was determined by passing the material through standardized sieves (2, 1, 0.5, 0.25, 0.125 and 0.063 mm). The <0.063 mm size fraction of diatomite was than analysed using a laser diffraction particle-size analyser (Fritsch Analysette 22 NanoTec Plus).

Chemical and mineralogical analysis

The chemical composition of the diatomite powder support was determined using X-ray fluorescence (XRF; Skyray Explorer7000). The mineralogical compositions of the crude diatomite (Dc), the 2 mm diatomite fraction (D_{2mm}), support diatomite (Ds) and the catalyst before and after the reduction process were determined using X-ray diffraction (XRD; Riyaku Miniflex diffractometer; Cu-*K*α radiation; scanning range: 10–70°2θ; scanning step: 0.02°2θ).

Fourier-transform infrared spectroscopy

Fourier-transform infrared (FTIR) spectra were obtained using a Perkin Elmer spectrometer connected to a computer in the mid-infrared (MIR) range of 400–4000 cm^{-1}. The spectra were collected from samples Ds (<63 μm) and D_{2mm} (2 mm diatomite fraction).

Thermal analysis

The thermal behaviour of diatomite was determined by thermogravimetric analysis/differential scanning calorimetry (TGA/DSC) using a Mettler-Toledo SDT-Q600 TA instrument from ambient temperature to 1100°C at a heating rate of 10°C min^{-1}.

Structural and morphological characteristics of the diatomite supports and the catalyst

The structural and morphological characteristics of the support and the catalyst were examined using scanning electron microscopy (SEM; Sirion 200, FEI Co.).

Textural properties of the support and the catalyst

The textural characterization of the support and the catalyst was carried out using adsorption isotherms; the specific surface area was obtained according to the Brunauer–Emmett–Teller (BET) method using a NOVA 1994-2010 instrument (Quantachrome Instruments version 11.0). The pore size and the pore volume of the samples, previously degassed at 250°C, were determined from the low-temperature nitrogen adsorption.

Results and discussion

Particle-size distribution of the crude diatomite

The particle-size distribution of the crude diatomite powder (Dc; Fig. 1) showed a D_{50} value (50 wt.% of the material) of <0.98 mm, a D_{10} value of ~0.14 mm and a D_{90} value of 1.8 mm. The particle-size distribution as assessed using a laser scattering particle-size distribution analyser (Fig. 2) to analyse the fine fraction of diatomite shows that almost 50% of the particles have diameters <4.22 μm, with 10% being <1.13 μm and 90% being <12.40 μm. Two main granulometric populations were noted: the first one at 3.2 μm and the second one at 11 μm, with volume percentages of 3.50% and 3.72%, respectively. The most dominant fraction is of micrometre size, associated with small amounts of particles sized in the nanometre range (<100 nm).

Chemical composition of the diatomite support

The crude diatomite powder (Dc; Table 1) is mainly composed of SiO_2 (79.38 wt.%), with lesser amounts of CaO and Al_2O_3 (8.55 and 2.02 wt.%, respectively). Minor amounts of K_2O, Na_2O and Fe_2O_3, considered to be fluxing agents, are also present (0.78, 0.59 and 0.97 wt.%, respectively). The SiO_2 and Fe_2O_3 contents of the support diatomite decreased from 79.38 and 0.97 wt.% to 66.35 and 0.24 wt.%, respectively. The CaO content increased from 8.55 to 16.81 wt.%, and the loss on ignition (LOI) values increased from 5.67 to 7.45 wt.% for the Ds and Dc samples, respectively. The LOI of the diatomite support (Ds; 7.45 wt.%) is attributed to the combustion of organic matters and the release of CO_2 from the decomposition of the carbonate minerals.

The chemical composition of the 15Ni/Ds-700 catalyst (Table 1) showed lower oxide mass ratios compared with the support diatomite. Specifically, the SiO_2, Al_2O_3 and CaO contents decreased from 79.98, 7.13 and 16.81 wt.% to 64.60, 1.92 and 13.24 wt.%, respectively, for the support and the catalyst, respectively. On the other hand, the content of NiO in the catalyst was 15 wt.%, confirming that impregnation was successful. The LOI value of the 15Ni/Ds-700 catalyst (2.16 wt.%) was significantly reduced, suggesting that combustion of organic matter was taking place during the catalyst calcination at 700°C.

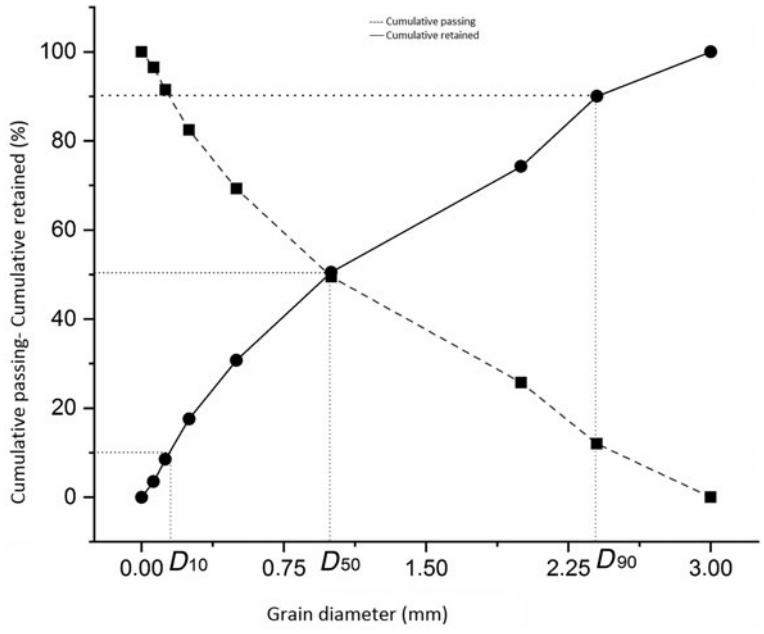

Figure 1. Particle-size distribution of the crude diatomite by dry sieving.

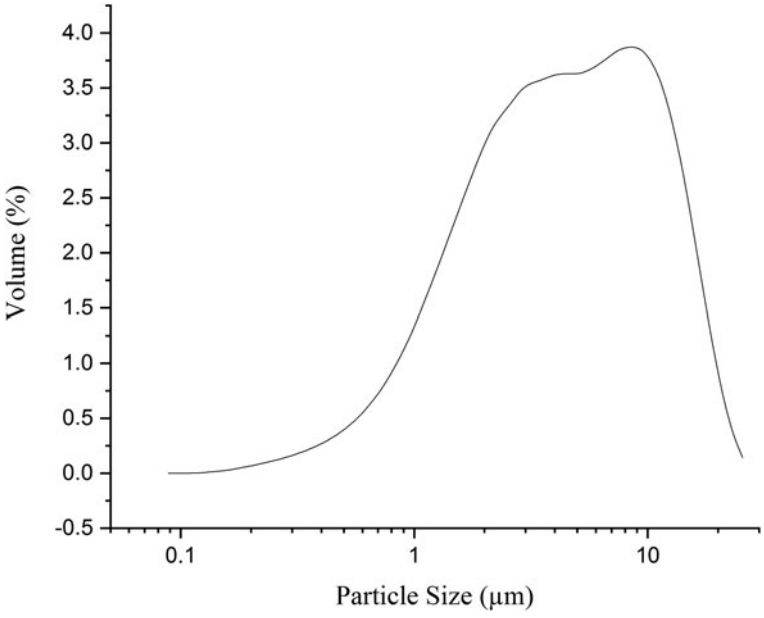

Figure 2. Particle-size distribution of the diatomite support.

Table 1. Chemical composition (wt.%) of the crude diatomite, support diatomite and 15Ni/Ds-700 catalyst.

Oxide	SiO_2	Al_2O_3	Fe_2O_3	CaO	MgO	K_2O	Na_2O	P_2O_5	TiO_2	NiO	LOI
Dc	79.38	2.02	0.97	8.55	1.73	0.78	0.59	0.10	0.20	–	5.67
Ds	66.35	7.13	0.24	16.81	1.28	0.39	0.25	0.07	0.02	–	7.45
15Ni/Ds-700	64.60	1.92	0.26	13.24	1.56	0.35	0.093	0.065	0.75	15.00	2.16

Mineralogical analysis of the diatomite

The XRD traces (Fig. 3) show that the crude diatomite (Dc) consists of amorphous SiO_2, characterized by a hump at 20–25°2θ. However, this hump diminished in the Ds support and disappeared in D_{2mm}. Quartz was identified in all of the samples (main peak at 26.85°2θ); quartz seems to have been better crystallized in the Ds sample compared to the Dc and D_{2mm} samples. Calcite ($CaCO_3$) and ankerite ($(Ca,Mg,Fe)CO_3$; Hadjar *et al.*, 2008; Aouadja *et al.*, 2022) were identified by peaks at 29.40 and 30.74°2θ, respectively, in all of the samples. The abundance of these phases diminished in the diatomite support (Ds).

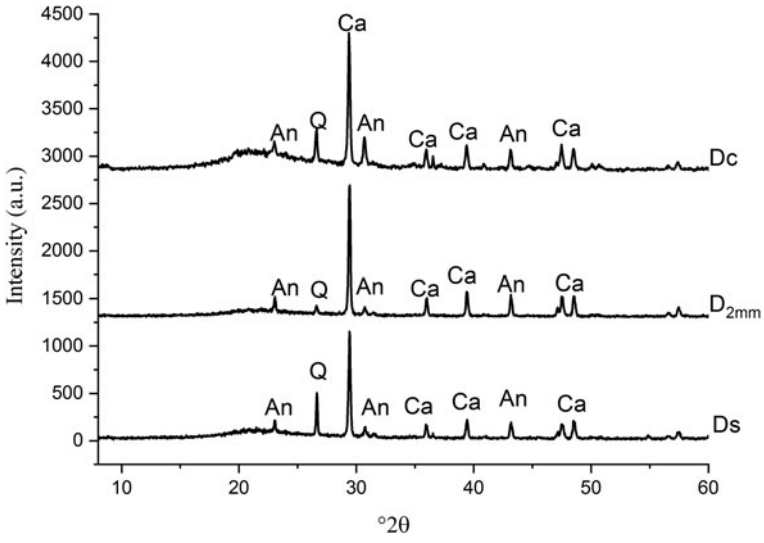

Figure 3. XRD traces of Dc, D_{2mm} and Ds. An = ankerite ($(Ca,Mg,Fe)CO_3$); Ca = calcite ($CaCO_3$); Q = quartz (SiO_2).

FTIR analysis

All of the functional groups assigned to calcite, ankerite, quartz and water were present in both Ds and D_{2mm} samples but at different band intensities (Fig. 4). The FTIR spectra of the Ds and D_{2mm} diatomite samples show the presence of CO_3^{2-} bands at 1431, 876 and 727 cm^{-1} from calcite and ankerite. The deformation band centred at 876 cm^{-1} is more accentuated in the Ds sample than in the D_{2mm} sample. The bands related to silica (Si–O–Si) occur at 1068 and 484 cm^{-1} for both samples at the same intensity. A large band centred at 3435 cm^{-1} and a weak one at 1637 cm^{-1} are attributed to the stretching and bending vibrations of the OH bond of the adsorbed water; they are slightlyS visible in the Ds sample. The silanol group SiO–H centred at 730 cm^{-1} is attributed to O–H deformation of the free silica, which is accentuated in the Ds sample.

Thermal analysis of the diatomite support

The results of coupled TGA/DSC are presented on Fig. 5. A total weight loss of 18.39% at 1180°C was recorded in three main steps. The first weight loss event (2.57 wt.%) associated with an endothermic peak at 62°C is due to dehydration of diatomite (absorbed moisture). The second weight loss event (2.68 wt.%) is associated with a large exothermic peak at 255°C due to the combustion of organic matter. The third weight loss event (13.14 wt.%), associated with a large endothermic peak at 720°C, is due to both dehydroxylation of silanol groups and carbonate decomposition (Giles *et al.*, 1974). Finally, a weak exothermic peak observed at 930°C is caused by the crystallization of diatomite.

Structural analysis of the diatomite support

The nitrogen adsorption–desorption isotherms of the diatomite support (Ds; Fig. 6) are type-IV isotherms, indicating the presence of both micropores and mesopores (Sun *et al.*, 2018). Based on the De Boer classification (De Boer, 1958), Ds is defined as a mesoporous solid incorporating cylindrical pores (Rabie *et al.*, 2019; Liu *et al.*, 2020).

The diatomite support had specific surface area, total pore volume and average pore diameter values of 46.33 $m^2\ g^{-1}$, 0.579 $cm^3\ g^{-1}$ and 26.55 nm, respectively. The diatomite support is a mesoporous

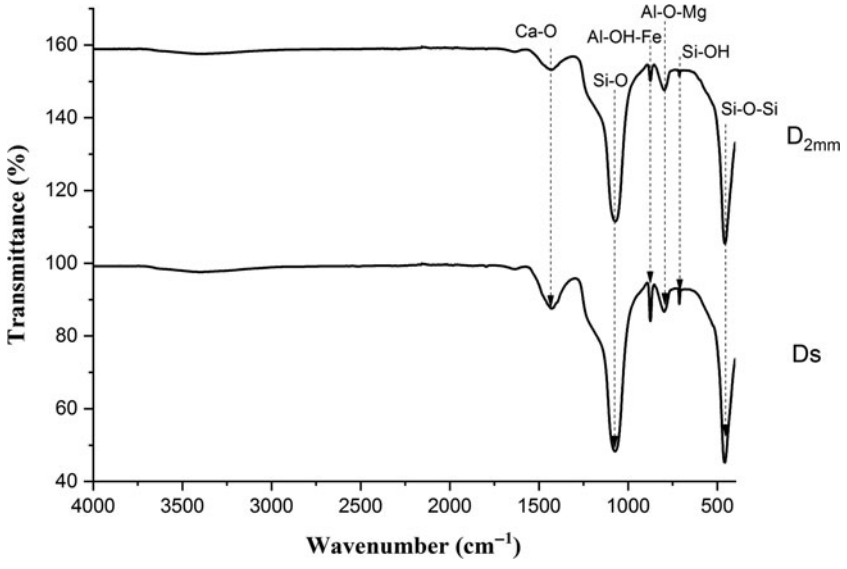

Figure 4. FTIR spectra of the D_{2mm} and Ds diatomite.

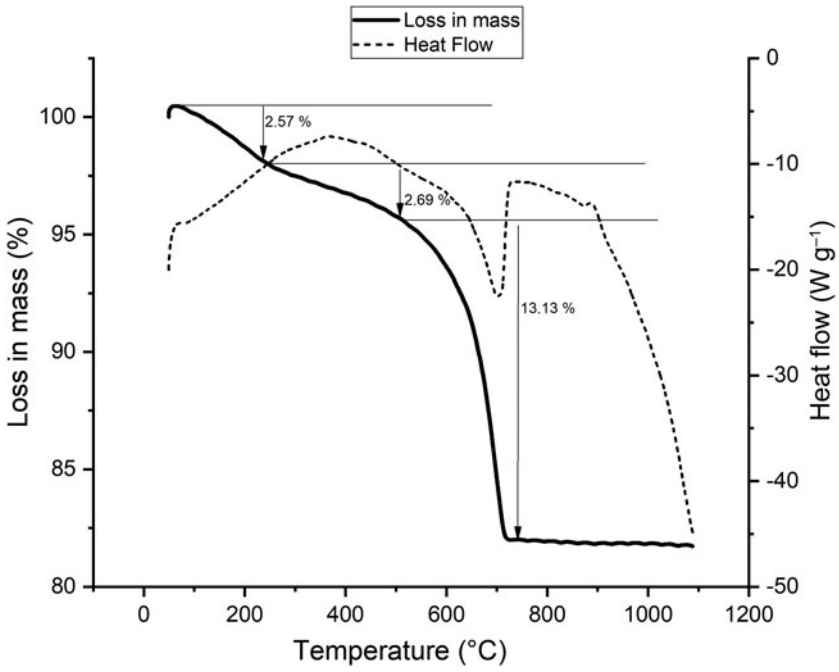

Figure 5. TGA/DSC analysis of the diatomite support.

material because the average pore diameter is between 2 and 50 nm (Chen *et al.*, 2021). The specific surface area of the diatomite used in this work was larger (46.33 m^2 g^{-1}) than that determined by Chen *et al.* (2021) for a Chinese diatomite (20.50 m^2 g^{-1}). In addition, the pore volume of the Algerian diatomite support (0.579 cm^3 g^{-1}) was larger and the pore size (26.55 nm) was smaller than those of the Chinese diatomite used by Chen *et al.* (2021; 0.084 cm^3 g^{-1} and 164.29 nm, respectively).

Catalyst characterization

XRD results of the catalyst before and after the reduction process

The XRD results of the catalyst material before the reduction process (Fig. 7) show that it consists mainly of calcite ($CaCO_3$), nickel oxide (NiO), feldspar and quartz. NiO was observed with an intense 020 peak at 43.22°2θ, which indicates impregnation of Ni in the pores and tunnels of the diatomite structure (Merkouri *et al.*, 2022). After reduction with H_2 for 4 h, the catalyst 15Ni/Ds-700 consisted of quartz (SiO_2), wollastonite ($CaSiO_3$), NiO and metallic nickel (Ni^0; Fig. 7). The presence of wollastonite is due to a reaction between CaO and SiO_2 during calcination at 700°C. Ni^0 is observed at ∼44.5 °2θ (111 plane), characterizing the active phase of the catalyst. By contrast, the incomplete reduction of Ni^{2+} in the catalyst leads to the presence of the NiO phase, which is identified by the peak at ∼43.6°2θ (Terekhova *et al.*, 2023).

These results are in agreement with the results obtained by Zhang *et al.* (2018), who prepared a Ni/MgOSiO_2 catalyst to

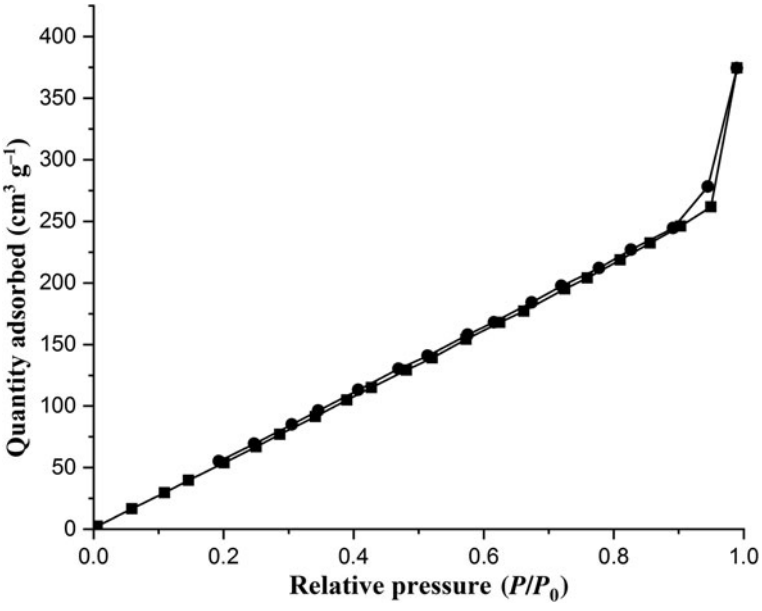

Figure 6. Nitrogen adsorption–desorption isotherms of the diatomite support. Squares represent results from the adsorption process and circles represent results from the desorption process.

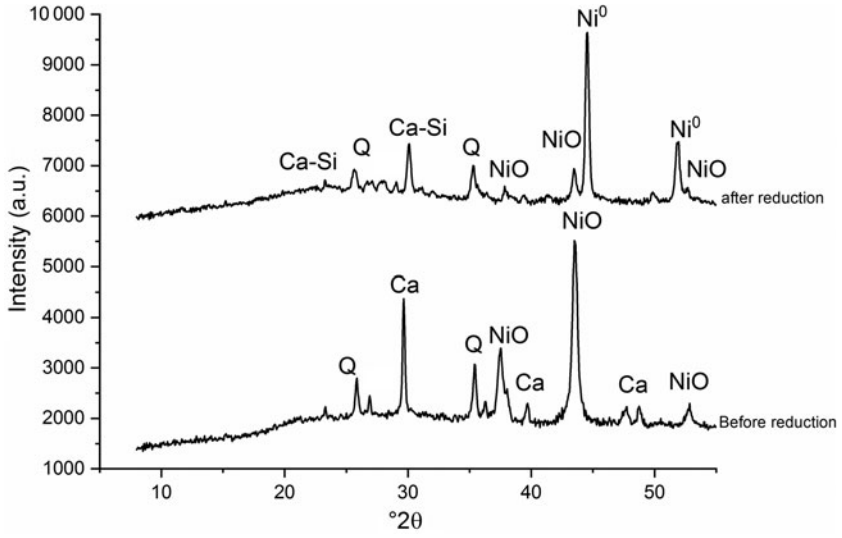

Figure 7. XRD traces of the catalyst material before and after the reduction process. Ca = calcite; Ca-Si = wollastonite ($CaSiO_3$); Ni^0 = metallic nickel; NiO = nickel oxide; Q = quartz.

improve the coking resistance of catalysts in DRM reactions. XRD analysis indicated a strong presence of NiO (peaks at ~39.7, 43.3 and 53.2°2θ). In addition, Ni^0 was identified from the peaks at ~44.5 and 51.8°2θ.

Textural analysis of the catalyst

The nitrogen adsorption–desorption isotherms of the catalyst supported on the diatomite powder are typical of type IV isotherms, indicating the presence of both micropores and mesopores (Fig. 8). The catalyst exhibited H3 hysteresis loops in the relative pressure (P/P_0) range 0.2–1.0. This is due to the filling of micropores belonging to the calcined diatomite support (Yao *et al.*, 2018; Zijie *et al.*, 2022). Consequently, the specific surface area (25.69 m^2 g^{-1}), pore volume (0.20 cm^3 g^{-1}) and pore size (15.72 nm) of the catalyst decreased compared to the support before impregnation. This is due to the calcination of the catalyst, which affects the structural characteristics blocking the pores after impregnation, and to the incorporation of NiO groups into the tunnels of the diatomite support (Sun *et al.*, 2018; Liu *et al.*, 2020).

Structural and morphological characteristics of the diatomite supports and the catalyst

The SEM images of the Dc diatomite powder showed the presence of continuous circular rings closely interconnected, forming a porous network structure with connected tunnels (Fig. 9a). The diatoms are of marine origin with a secondary, regular, circle-shaped structure (Hadjadj-Aoul *et al.*, 2005). However, the SEM images of the diatomite support Ds before the reduction process revealed the heterogeneous morphology of the grains within the diatomite (Fig. 9b). The pores are circular and have a regular-shaped structure with nanosized dimensions, yielding a high porosity of the support Ds. In addition, impurities surrounding the holes were observed. According to energy-dispersive X-ray spectroscopy (EDS) spectral analysis of a selected zone in the support

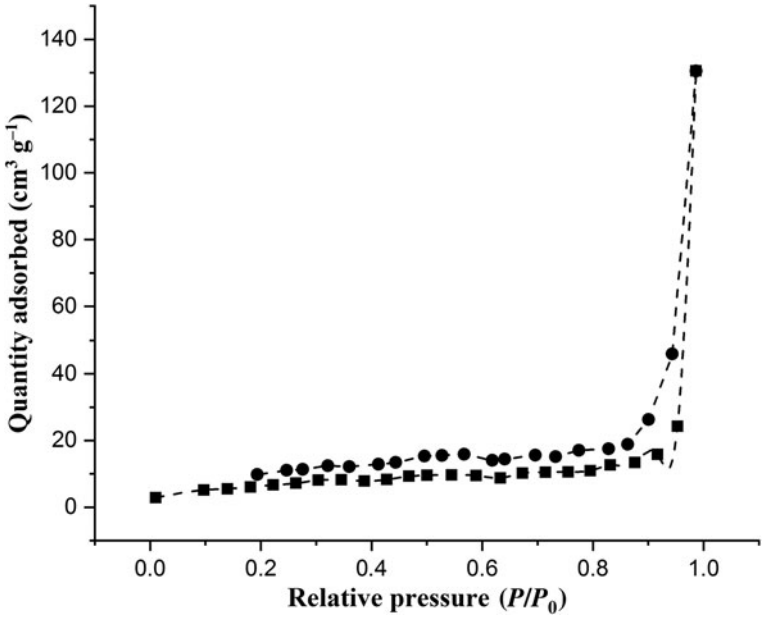

Figure 8. Nitrogen adsorption–desorption isotherms of the prepared catalyst. Squares represent results from the adsorption process and circles represent results from the desorption process.

Ds (Fig. 9c), Si, Ca and O are the main elements in the support. The small amounts of Ni, Mg and Al detected belong to the support, and they are considered to be impurities.

The SEM image of the catalyst after the reaction showed agglomerated and heterogeneously dispersed Ni particles distributed within the diatomite matrix, with almost 13% Ni on the sections and inside the orifices of selected grains (Fig. 9d). Elemental EDS analysis of the selected zone of the catalyst showed that the main elements were Si, Ca, O and Ni. The small amount of Au detected is attributed to contamination (Fig. 9e).

Catalytic performance tests

The XRD traces of the 15Ni/Ds-700 catalyst after the reaction demonstrated the presence of the Ni^0 metal phase obtained during the sintering of the catalyst identified from the peaks at 44.51 and 51.83°2θ belonging to the (111) and (200) planes, respectively (Fig. 10). Moreover, peaks of NiO were detected at 43 and 47.1°2θ, belonging to the (111) and (200) planes, respectively. A low-graphite carbon peak with a hexagonal structure appears at 26.38°2θ. The presence of Ni^0 and the limited formation of carbon after the reaction explains the high stability of the catalyst (Wang *et al.*, 2013; Bian *et al.*, 2016; Zhang *et al.*, 2018). Finally, peaks of quartz and calcite were still observed on the catalyst at 20.85 and 29.40°2θ, respectively; despite the reaction process and the sintering temperature, no phase transformations occurred.

The catalytic performance of the synthesized 15Ni/Ds-700 catalyst assessed according to the conversion rate of CH_4 and CO_2 was studied in the DRM process (Figs 11 & 12). The numerical results regarding conversion, product selectivity and H_2:CO ratio are given in Table 2, and Table 3 shows the theoretical carbon balance products and the activity of reactants and products.

The catalyst deposited on diatomite (15Ni/Ds-700) is active (Figs 11 & 12), showing CH_4 conversion of 14% and CO_2 conversion of 12%, with H_2 yields of 17%, CO yields of 37% and a H_2:CO ratio of 0.45 (Tables 2 & 3). Despite the physicochemical properties of the Ni catalyst supported on diatomite (fine Ni particle size, good dispersion of the active phase on the support and controlled pore volume), the conversion rates of CO_2 and CH_4 remained low at 700°C. This is probably due to the low reduction of NiO to Ni^0, which is the active phase, and the low specific surface area of the Ni/diatomite catalyst (25.69 $m^2\ g^{-1}$). A low rate of reduction of NiO was detected after XRD analysis of the samples

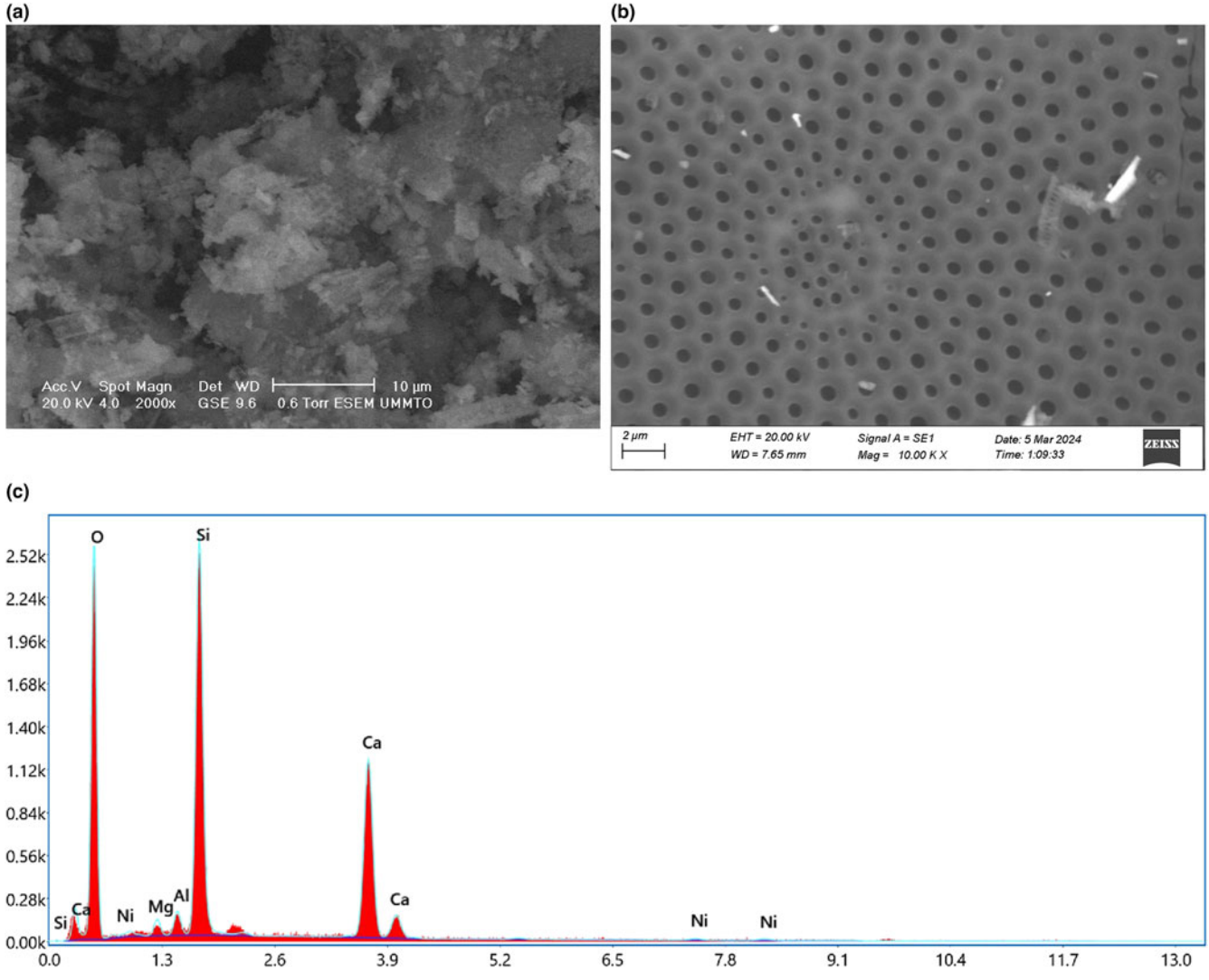

Figure 9. SEM images of (a) the diatomite support Ds and (b) the catalyst before the reduction process. (c) EDS spectrum of the diatomite support. (d) SEM image of the catalyst after the reaction process and (e) EDS spectrum of the catalyst after reaction.

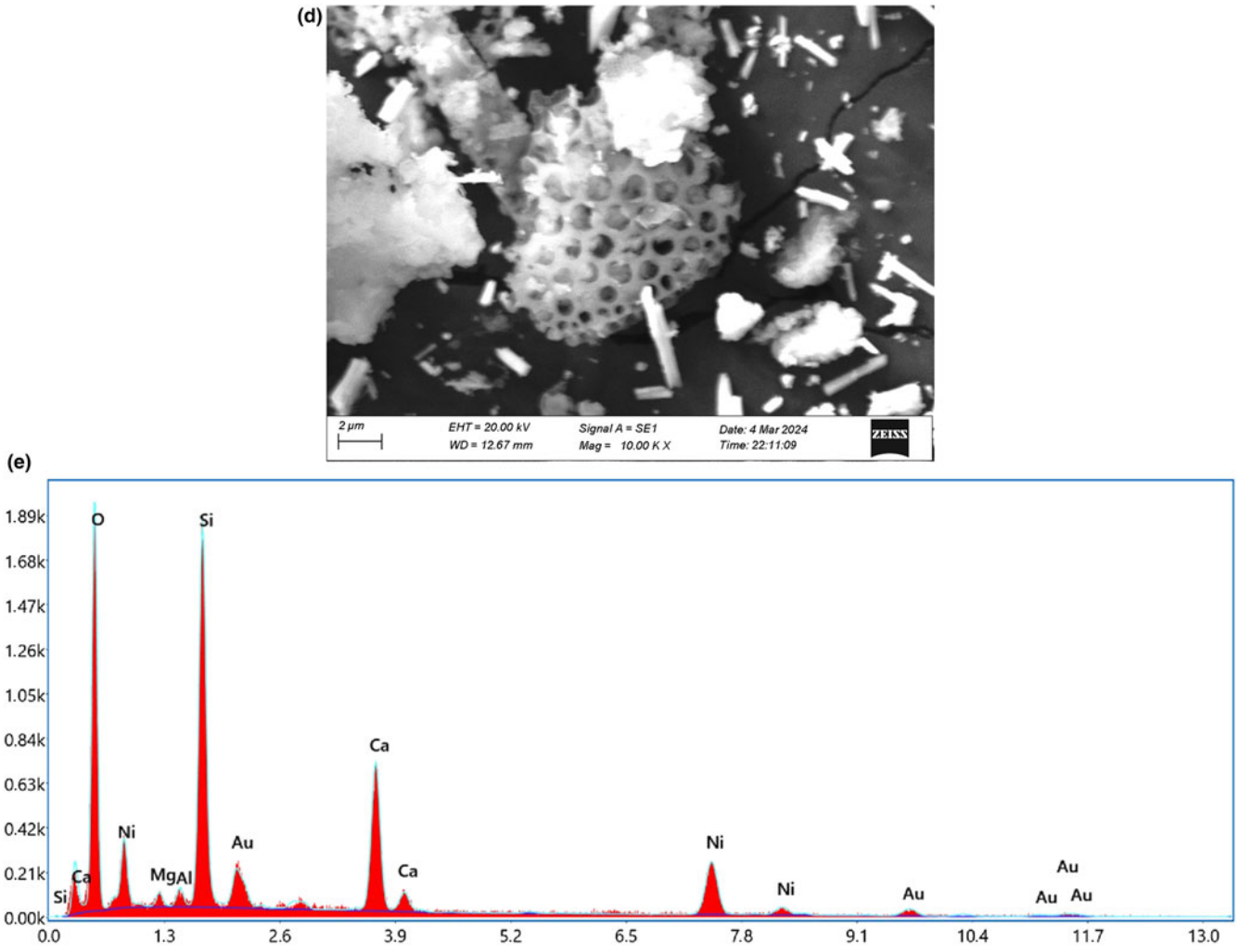

Figure 9. Continued.

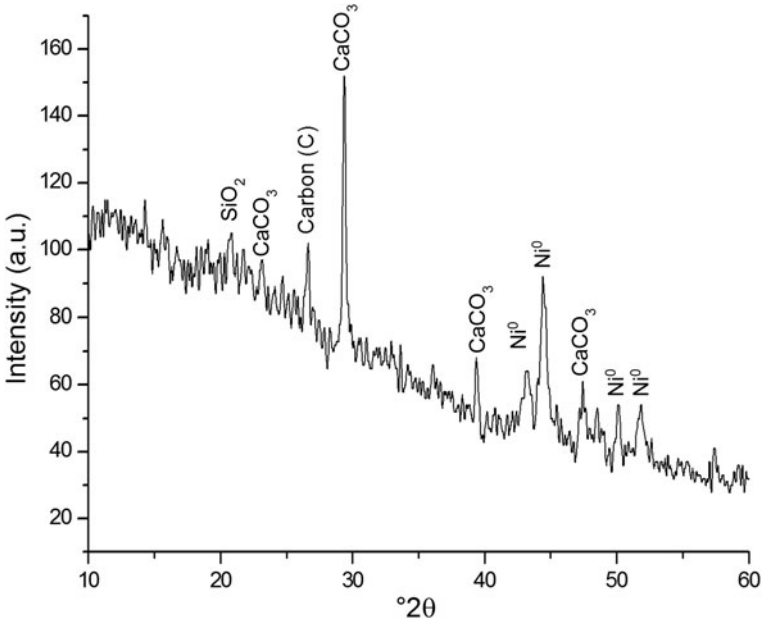

Figure 10. XRD trace of the catalyst (15Ni-Ds700) after the reaction process.

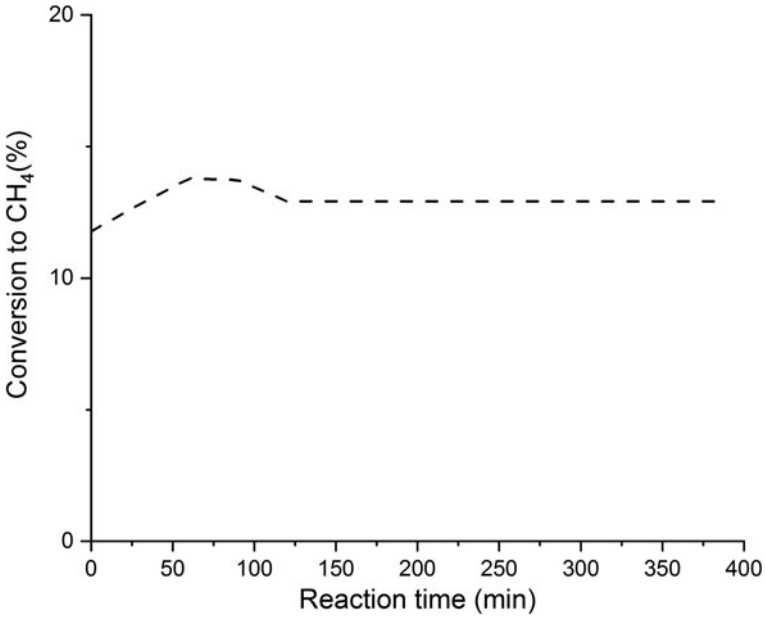

Figure 11. Conversion to CH_4 (%) as a function of reaction time.

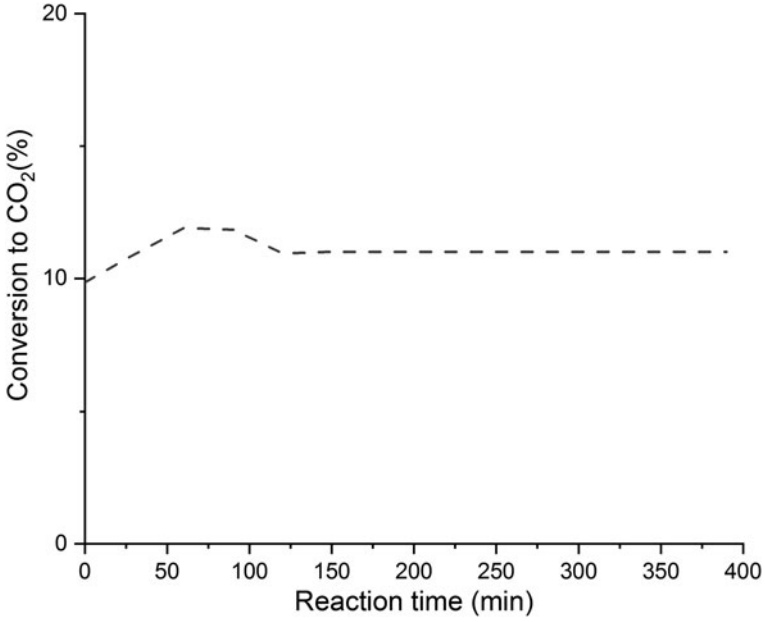

Figure 12. Conversion to CO_2 (%) as a function of reaction time.

Table 2. Conversion rate of the reagents (CH_4 and CO_2), selectivity of the products and the H_2:CO ratio as function of time of reaction of 15Ni/ Ds-700.

	Conversion rate (%)		Selectivity (%)			
Injection time (min)	CH_4	CO_2	H_2	CO	CO_2:CH_4	H_2:CO
0	12	10	16	44	0.89	0.36
30	13	11	15	41	0.91	0.36
60	14	12	15	38	0.92	0.39
90	14	12	14	36	0.92	0.38
120	13	11	14	37	0.91	0.38
150	13	11	14	37	0.91	0.38
180	13	11	14	37	0.91	0.38
210	13	11	14	37	0.91	0.38
240	13	11	14	37	0.91	0.38
270	13	11	14	37	0.91	0.38
300	13	11	14	37	0.91	0.38
330	13	11	14	37	0.91	0.38
360	13	11	14	37	0.91	0.38

Table 3. Theoretical balance of the carbonaceous products and the activities of the reagents and the products as a function of time of reaction of 15Ni/Ds-700.

Injection time (min)	Activity (μmol/g.s)				X_C
	CH_4	CO_2	CO	H_2	
0	0.74	0.66	0.61	0.24	93.92
30	0.80	0.73	0.63	0.25	93.05
60	0.87	0.80	0.63	0.25	92.07
90	0.86	0.80	0.60	0.24	91.87
120	0.81	0.74	0.58	0.23	92.53
150	0.81	0.74	0.58	0.23	92.53
180	0.81	0.74	0.58	0.23	92.53
210	0.81	0.74	0.58	0.23	92.53
240	0.81	0.74	0.58	0.23	92.53
270	0.81	0.74	0.58	0.23	92.53
300	0.81	0.74	0.58	0.23	92.53
330	0.81	0.74	0.58	0.23	92.53
360	0.81	0.74	0.58	0.23	92.53

reduced at 700°C. The XRD results of the catalyst after reduction with pure H_2 at 700°C (Fig. 10) showed the presence of the NiO phase; consequently, Ni^{2+} was not entirely reduced to Ni^0, thus explaining the low conversion rates of CH_4 and CO_2. The molar ratios of CO_2:CH_4 and H_2:CO could be used as indicators to determine the activity of the 15Ni/Ds-700 catalyst (Liu *et al.*, 2018). These ratios did not significantly vary for the catalyst, and they should be 1 for the DRM. The main disadvantage of Ni-based catalysts is the deposition of coke during the DRM process (Kristiani & Takeishi, 2022). However, the CO_2 conversions are higher than those of methane, which can be explained by the occurrence of the reverse secondary reaction of gas to water (Equation 9):

$$H_2 + CO_2 \rightarrow CO + H_2O \quad (9)$$

The presence of this reaction was confirmed by the low H_2:CO molar ratio, which yields some carbon deposition by either the Boudouard reaction (below 700°C) and/or CH_4 cracking reactions at high temperatures (Wang *et al.*, 1996; Zhang *et al.*, 2013).

In the present study, the 15Ni/Ds-700 recorded a low carbon deposition rate and stability during 6 h of the dry reforming reaction. The low conversion rate to reactive gases (CH_4 and CO_2) obtained (12%) is probably due to the partial reduction of NiO to Ni^0 (Figs 11 & 12).

The Ni-diatomite catalysts in dry reforming reactions achieved 90% CH_4 conversion when the Ni-diatomite was calcined at the 800°C (Jabbour *et al.*, 2015). In addition, the H_2:CO molar ratio was close to unity. These catalysts were also relatively stable during catalytic measurements carried out at 650°C for 12 h (Jabbour *et al.*, 2015). This is probably due to the reduction state of NiO to Ni^0 (Kristiani & Takeishi, 2022). The activity and stability of catalysts supported by diatomite depend on the heat treatment of the diatomite. This also affects the type of carbon formed after the reaction test. However, Pan *et al.* (2020) obtained 58% and 44% conversion rates to CH_4 and CO_2, respectively, using mesoporous silica-supported Ni or Ni–Pd bimetallic catalysts. The presence of noble metals was beneficial for reducing the size of the active metal particles and promoting their dispersion (Pan *et al.*, 2020). Furthermore, the stability of conversion to CH_4 and CO_2 depends on the amount of carbon deposition and consumption, which affect the activity and stability of the catalyst (Li *et al.*, 2017).

Furthermore, the catalyst used has a low rate of carbon deposition (carbon balance = 93%) and high stability for 6 h. This result is mainly due to the strong Ni support that generates the formation of well-dispersed Ni metal particles on the silica support, thereby enabling good catalytic activity and stability by inhibiting the sintering of Ni particles and carbon deposition. The results obtained are in accordance with those from a similar work that used natural silica as a support for perovskite-based catalysts: 20% $LaNiO_3/SiO_2$ and 40% $LaNiO_3/SiO_2$ (Sellam *et al.*, 2019).

Summary and conclusions

A diatomite support (Ds) obtained from sieving (<63 μm) of a crude Algerian diatomite (Dc) was used as a support for a Ni-based catalyst applied in the DRM reaction. The 15Ni/Ds-700 catalyst had lower SiO_2, Al_2O_3 and CaO contents than the support diatomite (79.98, 7.13 and 16.81 wt.% and 64.60, 1.92 and 13.24 wt.%, respectively). The NiO content of the catalyst was 15 wt.%, confirming successful impregnation. In addition, the specific surface area of Ds (46.33 $m^2\ g^{-1}$) was higher compared to Dc (26.47 $m^2\ g^{-1}$).

The 15Ni/Ds-700-supported catalysts were prepared according to the wet impregnation procedure. Their activity was tested in the DRM at 700°C. XRD analysis of the supported catalyst showed the presence of an NiO phase. The reduction of the Ni-based catalyst (NiO) to Ni^0 supported on diatomite was not complete because this process requires very high temperatures. The 15Ni/Ds-700 catalyst has a relatively low specific surface area (25.69 $m^2\ g^{-1}$) and small particle size (15.72 nm). Consequently, this catalyst exhibits low catalytic activity, which is attributed to the low specific surface area and low reducibility of NiO to Ni^0. A small NiO particle size, high dispersibility on the support and a successful reduction of NiO to Ni^0 might increase the catalytic activity.

The fine powder of Algerian diatomite (<63 μm) is a promising low-cost material; it might be used as a support for a Ni-based catalyst for DRM applications. However, it should be optimized through the addition of promoters and by increasing the temperature of reduction to avoid the formation of excess water during the reaction, which would cause deactivation of Ni^0. An increase in reduction temperature might lead to the total transformation of NiO to Ni^0. Furthermore, the addition of promoters (alkaline, alkaline earth or rare earth elements) holds promise for enhancing the basicity of the catalyst support.

Conflicts of interest. The authors declare none.

References

Abdullah N., Ainirazali N. & Ellapan H. (2021) Structural effect of Ni/SBA-15 by Zr promoter for H_2 production *via* methane dry reforming. *International Journal of Hydrogen Energy*, **46**, 24806–24813.

Aouadja F., Bouzerara F., Guvenc C.M. & Demir M.M. (2022) Fabrication and properties of novel porous ceramic membrane supports from the (Sig) diatomite and alumina mixtures. *Boletín de la SociedadEspañola de Cerámica y Vidrio*, **61**, 531–540.

Balaska A., Samar M.E., Meradi H., Abbess I.M. & Leksir Y.L.D. (2008) Caractérisation et étude thermique et morphologique de la diatomite Algérienne. Algerian Journal *of* Advanced Materials, **4**, 37–40.

Benayache S., Alleg S., Mebrek A. & Sunol J.J. (2018) Thermal and microstructural properties of paraffin/diatomite composite. Vacuum, **157**, 136–144.

Bian Z., Suryawinata I.Y. & Kawi S. (2016) Highly carbon resistant multicore–shell catalyst derived from Ni-Mg phyllosilicate nanotubes silica for dry reforming of methane. Applied Catalysis B: Environmental, **195**, 1–8.

Challiwala M.S., Ghouri M.M., Linke P., El-Halwagi M.M. & Elbashir N.O. (2017) A combined thermo-kinetic analysis of various methane reforming technologies: comparison with dry reforming. Journal of CO_2 Utilization, **17**, 99–111.

Chen L., Li Z., Li W., Chen Z., Chen G., Yang W. & Liu X. (2021) Investigation of adsorption kinetics and the isotherm mechanism of manganese by modified diatomite. ACS Omega, **6**, 16402–16409.

Cherrak R. & Hadjel M. (2016) Treatment of recalcitrant organic pollutants in water by heterogeneous catalysis using a mixed material (TiO2-diatomite of Algeria). Desalination and Water Treatment, **57**, 17139–17148.

De Boer J.H. (1958) *The Structure and Properties of Porous Materials*. Butterworths, London.

Dekkar S., Tezkratt S., Sellam D., Ikkour K., Parkhomenko K., Martinez-Martin A. & Roger A.C. (2020) Dry reforming of methane over Ni–Al_2O_3 and Ni–SiO_2 catalysts: role of preparation methods. Catalysis Letters, **150**, 2180–2199.

Fraine Y., Seladji C. & Aït-Mokhtar A. (2019) Effect of micro encapsulation phase change material and diatomite composite filling on hygrothermal performance of sintered hollowbricks. Building and Environment, **154**, 145–154.

Giles C.H., Smith D. & Huitson A. (1974) A general treatment and classification of the solute adsorption isotherm. I. Theoretical. Journal of Colloid and Interface Science, **47**, 755–765.

Hadjadj-Aoul O., Belabbes R., Belkadi M. & Guermouche M.H. (2005) Characterization and performances of an Algerian diatomite-based gas chromatography support. Applied Surface Science, **240**, 131–139.

Hadjar H., Hamdi B. & Ania C.O. (2011) Adsorption of p-cresol on novel diatomite/carbon composites. Journal of Hazardous Materials, **188**, 304–310.

Hadjar H., Hamdi B., Jaber M., Brendlé J., Kessaissia Z., Balard H. & Donnet J.B. (2008) Elaboration and characterisation of new mesoporous materials from diatomite and charcoal. Microporous and Mesoporous Materials, **107**, 219–226.

Hao J., Dai Z., Guan M., Dang P., Wang H., Yan C. & Li G. (2021) Simultaneous enhancement of luminescence and stability of lead halide perovskites by a diatomite microcavity for light-emitting diodes. Chemical Engineering Journal, **417**, 128056.

Jabbour K., El Hassan N., Davidson A., Massiani P. & Casale S. (2015) Characterizations and performances of Ni/diatomite catalysts for dry reforming of methane. Chemical Engineering Journal, **264**, 351–358.

Kristiani A. & Takeishi K. (2022) CO_2 methanation over nickel-based catalyst supported on yttria-stabilized zirconia. Catalysis Communications, **165**, 106435.

Lauermannová A.M., Lojka M., Jankovský O., Faltysová I., Pavlíková M., Pivák A. *et al.* (2021) High-performance magnesium oxychloride composites with silica sand and diatomite. Journal of Materials Research *and* Technology, **11**, 957–969.

Li B., Wang T., Le Q., Qin R., Zhang Y. & Zeng H.C. (2022) Surface reconstruction, modification and functionalization of natural diatomites for miniaturization of shaped heterogeneous catalysts. Nano Materials Science, **5**, 293–311.

Li L., Jiang X., Wang H., Wang J., Song Z., Zhao X. & Ma C. (2017) Methane dry and mixed reforming on the mixture of bio-char and nickel-based catalyst with microwave assistance. Journal of Analytical and Applied Pyrolysis, **125**, 318–327.

Liu D., Yu W., Deng L., Yuan W., Ma L., Yuan P. & He H. (2016) Possible mechanism of Pavlík structural incorporation of Al into diatomite during the deposition process I. *Via* a condensation reaction of hydroxyl groups. Journal of Colloid and Interface Science, **461**, 64–68.

Liu H., Yao L., Taief H.B.H., Benzina M., Da Costa P. & Gálvez M.E. (2018) Natural clay-based Ni-catalysts for dry reforming of methane at moderate temperatures. Catalysis Today, **306**, 51–57.

Liu M.Y., Zheng L., Lin G.L., Ni L.F. & Song X.C. (2020) Synthesis and photocatalytic activity of BiOCl/diatomite composite photocatalysts: natural porous diatomite as photocatalyst support and dominant facets regulator. Advanced Powder Technology, **31**, 339–350.

Mansour B., Bessedik M., Saint Martin J.P. & Belkebir L. (2008) Signifcation paléoécologique des assemblages de diatomées du Messinien du Dahra sud-occidental (bassin du Chélif, Algérie nord-occidentale). Geodiversity, **30**, 117–139.

Mendoza-Nieto J.A., Duan Y. & Pfeiffer H. (2018) Alkaline zirconates as effective materials for hydrogen production through consecutive carbon dioxide capture and conversion in methane dry reforming. Applied Catalysis B: Environment and Energy, **238**, 576–585.

Meradi H., Bahloul L., Boubendira K., Bouazdia A. & Ismail F. (2015) Characterization by thermal analysis of natural kieselguhr and sand for industrial application. Energy Procedia, **74**, 1282–1288.

Merkouri L.P., Le Saché E., Pastor-Pérez L., Duyar M.S. & Reina T.R. (2022) Versatile Ni–Ru catalysts for gas phase CO_2 conversion: bringing closer dry reforming, reverse water gas shift and methanation to enable end-products flexibility. Fuel, **315**, 123097.

Moreno A.A., Ramirez-Reina T., Ivanova S., Roger A.C., Centeno M.A. & Odriozola J.A. (2021) Bimetallic Ni–Ru and Ni–Re catalysts for dry reforming of methane: understanding the synergies of the selected promoters. Frontiers in Chemistry, **9**, 694976.

Niu J.T., Wang Y.L., Liland S.E., Regli S.K., Yang J. & Rout K.R. (2021) Unraveling enhanced activity, selectivity, and coke resistance of Pt–Ni bimetallic clusters in dry reforming. ACS Catalysis, **11**, 2398–2411.

Pakhare D. & Spivey J. (2014) A review of dry (CO_2) reforming of methane over noble metal catalysts. Chemical Society Reviews, **43**, 7813–7837.

Pan C., Guo Z., Dai H., Ren R. & Chu W. (2020) Anti-sintering mesoporous Ni–Pd bimetallic catalysts for hydrogen production *via* dry reforming of methane. International Journal of Hydrogen Energy, **45**, 16133–16143.

Qin Z.Z., Chen J., Xie X.L., Luo X., Su T.M. & Ji H.B. (2020) CO_2 reforming of CH_4 to syngas over nickel-based catalysts. Environmental Chemistry Letters, **18**, 997–1017.

Rabie A.M., Shaban M., Abukhadra M.R., Hosny R., Ahmed S.A. & Negm N.A. (2019) Diatomite supported by CaO/MgO nanocomposite as heterogeneous catalyst for biodiesel production from waste cooking oil. Journal of Molecular Liquids, **279**, 224–231.

Raje A.P., O'Brien R.J. & Davis B.H. (1998) Effect of potassium promotion on iron-based catalysts for Fischer–Tropsch synthesis. Journal of Catalysis, **180**, 36–43.

Sellam D., Ikkour K., Dekkar S., Messaoudi H., Belaid T. & Roger A.C. (2019) CO_2 reforming of methane over $LaNiO_3$ perovskite supported catalysts: influence of silica support. Bulletin of Chemical Reaction Engineering & Catalysis, **14**, 568–578.

Shen Z., Wang H., Yu Q., Li Q., Lu X. & Kong X. (2021) On-site separation and identification of polycyclic aromatic hydrocarbons from edible oil by TLC-SERS on diatomite photonic biosilica plate. Microchemical Journal, **160**, 105672.

Sophiana I.C., Iskandar F., Devianto H., Nishiyama N. & Budhi Y.W. (2022) Coke-resistant Ni/$CeZrO_2$ catalysts for dry reforming of methane to produce hydrogen-rich syngas. Nanomaterials, **12**, 1556.

Sun M., Chen W.C., Zhao L., Wang X.L. & Su Z.M. (2018) A PTA/MIL-101 (Cr)-diatomite composite as catalyst for efficient oxidative desulfurization. Inorganic Chemistry Communications, **87**, 30–35.

Taoukil D., El Meski Y., Lahlaouti M.I., Djedjig R. & El Bouardi A. (2021) Effect of the use of diatomite as partial replacement of sand on thermal and mechanical properties of mortars. Journal of Building Engineering, **42**, 103038.

Terekhova E.N., Belskaya O.B., Trenikhin M.V., Babenko A.V., Muromtzev I.V. & Likholobov V.A. (2023) Nickel catalysts based on carbon-mineral supports derived from sapropel for hydroliquefaction of sapropel organic matter. Fuel, **332**, 126300.

Van Viet P., Van Chuyen D., Hien N.Q., Duy N.N. & Thi C.M. (2020) Visible-light-induced photo-Fenton degradation of rhodamine B over Fe_2O_3–diatomite materials. Journal of Science: Advanced Materials and Devices, **5**, 308–315.

Wang N., Yu X., Shen K., Chu W. & Qian W. (2013) Synthesis, characterization and catalytic performance of MgO-coated Ni/SBA-15 catalysts for methane dry reforming to syngas and hydrogen. International Journal of Hydrogen Energy, **38**, 9718–9731.

Wang S., Lu G.Q. & Millar G.J. (1996) Carbon dioxide reforming of methane to produce synthesis gas over metal-supported catalysts: state of the art. Energy & Fuels, **10**, 896–904.

Xia K., Liu X., Chen Z., Fang L., Du H. & Zhang X. (2020) Efficient and sustainable treatment of anionic dye wastewaters using porous cationic diatomite. Journal of the Taiwan Institute of Chemical Engineers, **113**, 8–15.

Yao G., Lei J., Zhang X., Sun Z. & Zheng S. (2018) One-step hydrothermal synthesis of zeolite X powder from natural low-grade diatomite. Materials, **11**, 906.

Yusan S., Bampaiti A., Aytas S., Erenturk S. & Aslani M.A. (2016) Synthesis and structural properties of ZnO and diatomite-supported ZnO nanostructures. Ceramics International, **42**, 2158–2163.

Zhang C., Zhu W., Li S., Wu G., Ma X., Wang X. & Gong J. (2013) Sintering-resistant Ni-based reforming catalysts obtained *via* the nano confinement effect. Chemical Communications, **49**, 9383–9385.

Zhang Q., Feng X., Liu J., Zhao L., Song X., Zhang P. & Gao L. (2018) Hollow hierarchical Ni/MgO–SiO_2 catalyst with high activity, thermal stability and coking resistance for catalytic dry reforming of methane. International Journal of Hydrogen Energy, **43**, 11056–11068.

Zijie R., Yuhao H., Renji Z., Zhengzheng G., Huimin G., Xiangliang H. *et al*. (2022) The preparation and characterization of calcined diatomite with high adsorption properties by CaO hydrothermal activation. Colloids and Surfaces A: Physicochemical and Engineering Aspects, **636**, 128–134.